Naphtho[2,3-*a*]pyrene Thin Films – H,I, or J? Aggregate Alphabet Soup

Colette M. Sullivan[1], Adrienn M. Szucs[2], Theo Siegrist[2,3], and Lea Nienhaus[1,4]*

[1] Rice University, Department of Chemistry, Houston, TX, 77005

[2] National High Magnetic Field Laboratory, Tallahassee, FL 32310, USA

[3] FAMU-FSU College of Engineering, Tallahassee, FL 32310, USA

[4] Rice Advanced Materials Institute, Rice University, Houston, TX, 77005

*corresponding author: nienhaus@rice.edu

ABSTRACT

Photon upconversion within the solid state has the potential to improve existing solar and imaging technologies due to its achievable efficiency at low power thresholds. However, despite considerable advancements in solution-phase upconversion, expanding the library of potential solid-state annihilators and developing a fundamental understanding of their solid-state behaviors remains challenging due to intermolecular couplings affecting the energy landscape. Naphtho[2,3-*a*]pyrene has shown promise as a suitable solid-state annihilator; however, the origin of the underlying emissive features remains unknown. To this point, here, we investigate NaPy/polymethylmethacrylate thin films at varying concentrations to tune the intermolecular coupling strength to determine its photophysical properties. The results suggest that the multiple emissive features present at room temperature arise from an I-aggregate (520 nm), an excimer (550 nm), and a strongly coupled J-dimer (620 nm).

TOC Graphic

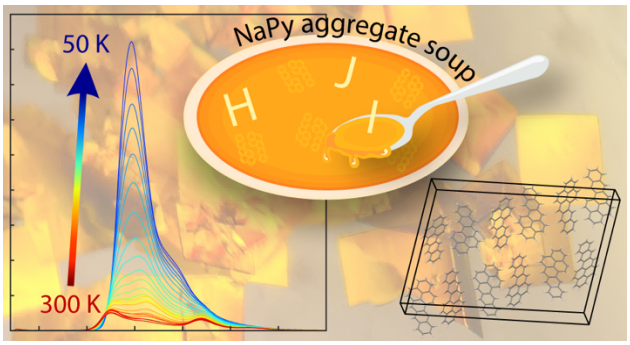

INTRODUCTION

Solid-state infrared-to-visible upconversion (UC) bears promise in applications including solar energy, anti-counterfeiting and infrared sensing and imaging.[1–5] Triplet-triplet annihilation upconversion (TTA-UC) is particularly promising for low-light applications since it can become efficient at low light intensities. Due to the low direct absorption cross sections of spin-triplet states upconversion systems consist of two parts: a triplet sensitizer and the annihilator.[6–14] In case of perovskite-sensitized upconversion, the perovskite sensitizes the triplet state of the annihilator by charge transfer, akin to an in-situ upconversion light emitting diode.[15–18] While absorbance up to 60% of the incident light a has been achieved, the annihilator library must be expanded. Currently, rubrene, the 'drosophila of upconversion' is the most utilized annihilator in solid-state devices.[18–24] However, the inherent ~0.4 eV energy loss during triplet sensitization limits the achievable apparent anti-Stokes shift.[25] Hence, recent efforts have been focusing on finding new annihilators to increase the energy of the emitted light.[26–28]

We have recently introduced naphtho[2,3-*a*]pyrene (NaPy) as a viable annihilator for perovskite-sensitized TTA-UC[28] To date, the photophysical properties of NaPy have not been well explored. With both the tetracene and pyrene backbone moieties, it a molecule with possibly rich photophysical properties, particularly with respect to solid-state applications.

Interesting results have been observed via scanning tunneling microscopy, where NaPy is shown to self-assemble on gold surfaces in chiral domains.[29,30] In addition, one study has suggested NaPy forms an unusual non-emissive J-aggregate.[31] As our previous results indicate an emissive nature of the excited state of NaPy in all forms - from isolated molecules in solution to ordered single crystals - a deeper dive into the underlying photophysical properties of NaPy is required to unravel the nature of the emissive state. In addition, our previous study indicates the presence of multiple emissive states which we had referred to as S_1' and S_1'' in the initial study due to their unknown underlying nature.[28] The ratio of these two emissive states differed based on the degree of underlying crystallinity: 'amorphous', crystallite, and single crystal. However, to date, the nature of these emissive states has not yet been investigated in detail.

Polyacenes have rich photophysical properties, particularly upon condensation into the solid state, where the intimate interactions can cause shifts in the absorption/emission properties, induce singlet fission or aggregation-related effects.[32–35] In polyacene thin films, the originally planar acene backbones can be present in twisted or planar confirmations depending upon the underlying molecular arrangement, resulting in variations of the triplet T_1 and singlet S_1 energy manifolds, which

in turn can influence recombination rates, rates of singlet fission and triplet-triplet annihilation. Furthermore, disorder can result in symmetry breaking, facilitating effects like singlet fission or TTA-UC.[36–39] Electronic coupling between adjacent molecules is also known to impact the optical transitions. Weak coupling results in a simple lowering of the transition energy manifesting as a redshift of the absorption spectrum. Furthermore, crystallization can result in stronger coupling between adjacent molecules. H-type aggregation causes a hypsochromic shift, while J-type aggregation results in a bathochromic shift of the absorption spectrum.[35,40] In addition, H-type aggregation generally suppresses emission, while J-aggregates generally feature superradiant emission with a low Stokes shift, high quantum yields, and fast radiative recombination rates.[40,41]

However, while conventional H- and J-aggregates sufficiently describe one dimensional aggregate structures, the strict distinction can fail in multidimensional aggregates, as both H- and J-type coupling can be present simultaneously. The herringbone nature of the crystal structure most solid polyacenes requires additional factors to be considered.[41] Caram and coworkers have therefore introduced an I-aggregate to describe a two-dimensional aggregate where J-type coupling is present along one direction of the aggregate, while H-type coupling is present along the orthogonal direction, with the magnitude dependent on the degree of slip stacking.[34] Here, the short-range coupling is H-type (positive), while the long-range coupling is J-type (negative). However, the magnitude of the positive coupling is smaller than that of the negative coupling, leading to a net bathochromic shift of the absorption of the aggregate. In addition to extended aggregates, strongly coupled localized excited state H- or J-type dimers can be present.[42,43]

Beyond H-, I- ,and J-type coupling between monomers, excimer formation is also possible. In contrast to aggregation-based effects which influence both the electronic ground state and excited state, the excited state dimer, or excimer, only exists within the excited state.[44,45] The ground state is dissociative; hence, the steady-state absorption spectrum is not influenced by excimer formation. However, the emission is shifted to lower energies than the monomer and is commonly broad and featureless.[46,47] The exact molecular structure of an excimer state is not commonly known but is often depicted as a pair of aligned molecules.

To understand the role of aggregation, dimer formation, and monomer emission in NaPy and unravel the underlying photophysics of the molecule in different local environments, we investigated how the properties of NaPy change when going from the isolated molecule in solution to the ordered molecular structure in the single crystal. To minimize the possible effects going from solvent to solid state, we mimic the isolated nature of the solution by combining the NaPy solution with a

polymethylmethacrylate (PMMA) matrix to ensure spacing between individual molecules. By increasing the NaPy loading in the PMMA matrix, we can investigate the impact of NaPy concentration on the photophysical properties.

Our results indicate that the multiple emissive states present in previously investigated NaPy thin films stem from the aggregate at 520 nm, the excimer at 550 nm and a strongly coupled redshifted J-dimer (J-coupled excimer) at 620 nm.

RESULTS AND DISCUSSION

Figure 1a shows the absorption spectrum of NaPy thin films spin coated from a 1.7 – 24.8 mM solution of NaPy in a PMMA matrix and a spin coated thin film of the stock NaPy solution (33.0 mM). As expected, the spectra show a slight redshift of the 0-0 vibronic feature at ~460 nm, caused by increasing intermolecular coupling due to a smaller average intermolecular distance due to the increased concentration. More interestingly, an additional redshifted absorption feature with strong oscillator strength appears for the three highest concentrations 18.2 – 33.0 mM, indicating J-type or I-type aggregation.[34,41,48] The corresponding emission spectra are depicted in Figure 1b. A clear change in the emissive states is found as the concentration is increased. NaPy in solution shows the expected vibronic progression with ν = 0.17 eV, resulting in features at 463, 494, 528, and 570 nm. In addition, a small blue-shifted feature appears at 441 nm, assigned to H-band emission. Interestingly, despite negligible changes in the absorption spectrum, the emission spectrum changes greatly when increasing the NaPy concentration to 8.3 mM NaPy/PMMA. The vibronic progression becomes much less distinct, and the spectrum significantly broadens (vide supra). Further increase of the concentration to 16.5 mM NaPy/PMMA results in a broad featureless emission spectrum. In agreement with the unaltered absorption spectrum at this concentration corresponding to the ground state, this broad emission can be attributed to the NaPy excimer, which exists only within the excited state. A minor increase of the concentration from 16.5 to 18.2 mM NaPy/PMMA causes another drastic change to the emission spectrum. The emission narrows and blueshifts, resulting in a small Stokes shift of 0.07 eV, as predicted for J-type aggregation. In addition, a small shoulder is present at 560 nm, the previously determined excimer emission wavelength. Upon further increasing the NaPy concentration to 24.8 and 33.0 mM, growth of an additional redshifted feature at 620 nm with an apparent vibronic progression at ~670 nm (ν = 0.15 eV) is observed. This is in agreement with our previous result, where we observed an increase in the red-shifted emission at 620 when going from a spin-coated thin film to a microcrystalline film and a single crystal: with increasing

crystallinity and increasing aggregate absorption feature, the feature at 620 nm increases in intensity.[28] To highlight changes in the photoluminescence (PL) intensity, the emission intensity normalized to the absorbance at the excitation wavelength of 405 nm is shown in the Supporting Information Figure S1.

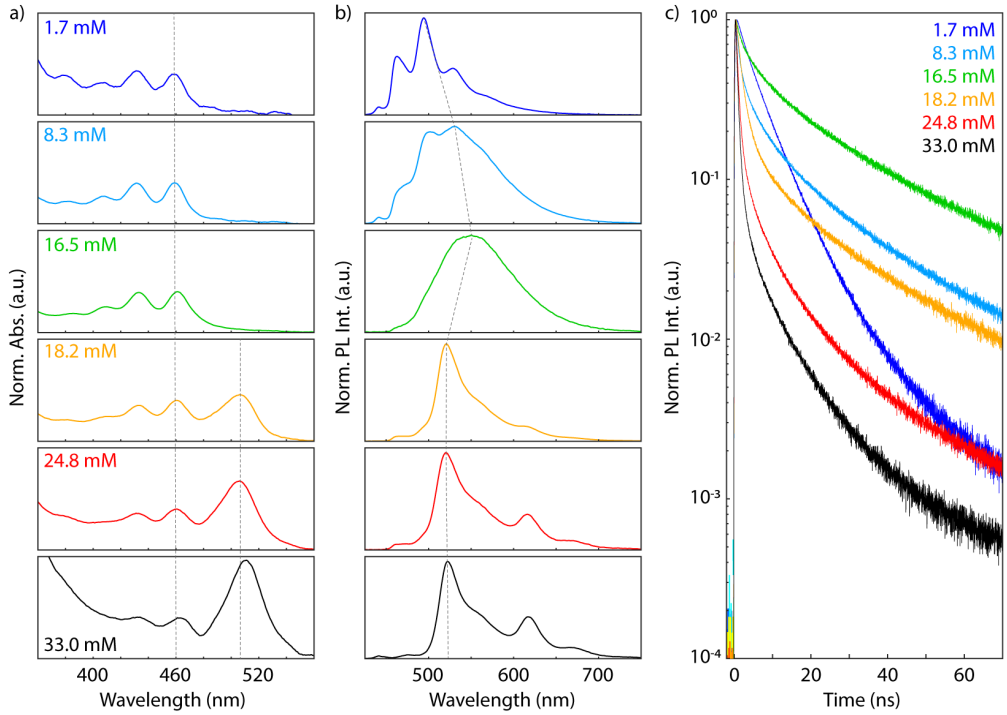

Figure 1: a) Normalized absorption and b) direct photoluminescence (PL) for the different NaPy/PMMA thin films collected under 405 nm excitation (30 W cm^{-2}). The grey dotted lines are included as guides to the eye. c) PL decays for the NaPy/PMMA films collected under 405 nm pulsed excitation (1 MHz, 64.9 mW cm^{-2}).

The corresponding fluorescence decay dynamics are shown in Figure 1c. To capture the rich dynamics of the disordered system and facilitate direct comparison, in the following, the decay dynamics are fit to triexponential decays unless otherwise noted.

$$I(t) = A_1 \exp\left(-\frac{t}{\tau_1}\right) + A_2 \exp\left(-\frac{t}{\tau_2}\right) + A_3 \exp\left(-\frac{t}{\tau_3}\right)$$

The extracted amplitude-weighted average lifetimes $\tau_{ave} = \frac{\sum_i A_i \tau_i}{A_i}$ for these samples are tabulated in Table 1 (Table S1). An interesting trend is found: the decay for the lowest NaPy concentration, which is 'monomer-like' appears nearly monoexponential. As the concentration is increased, the early time decay rate increases, possibly due to intermolecular energy transfer between the emissive states. As the fraction of excimer emission is increased, the PL decay dynamics become more multiexponential and the lifetime elongates, with the longest lifetime correlated to the pure excimer emission. Further

increase in NaPy concentration results in a concurrent shortening of the lifetime, as expected due to the fast recombination rates expected in aggregates, with the fastest lifetime correlated to the 33.0 mM spin-coated NaPy film (compare Figure 1c).

Table 1: Amplitude-weighted average lifetimes for the NaPy/PMMA thin films depicted in Figure 1 based on a triexponential fit. *Four exponentials were needed to fully capture the decay.

Concentration / mM	τ_{ave} / ns
1.7	6.3
8.3	4.8*
16.5	14.8
18.2	4.1
24.8	1.3
33.0	0.9

To highlight the morphology of the NaPy aggregates, a photograph of NaPy single crystals are shown in Figure 2a. Scanning electron microscopy (SEM) secondary electron (SE) images of a NaPy thin film drop cast (left) and spin coated (right) from the 33.0 mM stock solution are shown in Figure 2b. For the spin-coated film, initial nucleation is followed by two-dimensional ribbon-type growth feathering out from the nucleation site. Increasing the growth time by slow evaporation of the solvent by drop casting results in square platelet-like growth, highlighting that crystal growth occurs in a preferential direction. To verify that the square platelets are not unique to the drop casting method, Figure S2 shows a different region of the spin-coated NaPy film showing both square platelets as well as the ribbons feathered out from the nucleation sites. Single crystal X-ray diffraction of the crystals shown in Figure 2a reveals a P21/c space group, and the unit cell is shown in Figure 2c (the full unit cell parameters are listed in Table S2). The powder X-ray diffraction (Figure 2d) of the thin films yields reflections that are not consistent with expected positions based on single crystal structure (SI Figure S2), which is either due to residual solvent inclusion or a different polymorph. Furthermore, the thin film is highly textured, with a d-spacing perpendicular to the film of d(001) = 13.807(3) Å (at room temperature of 295 K). The precise crystal structure resulting in the powder pattern could not be solved due to the low number of observed reflections due to preferred orientations.

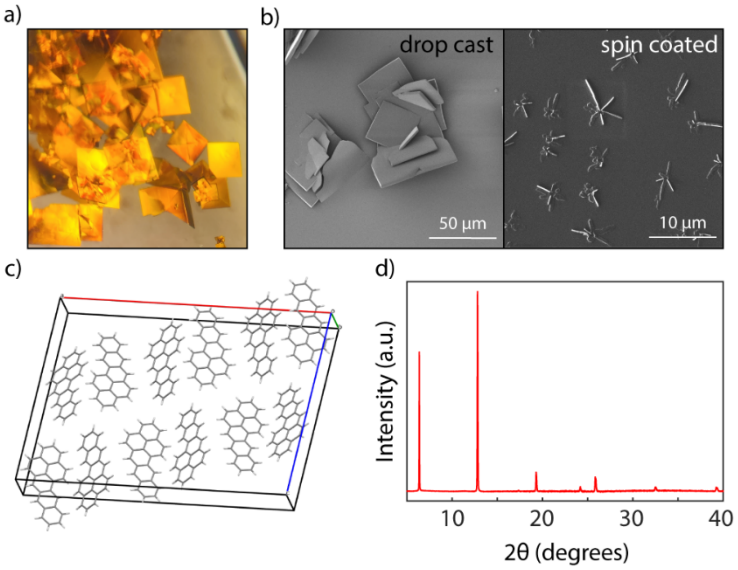

Figure 2: a) Photograph of NaPy single crystals. b) SEM-SE micrographs of a drop cast and spin coated NaPy thin film. c) NaPy single crystal structure obtained by single crystal X-ray diffraction highlighting the herringbone pattering in the P21/c space group. d) Room temperature NaPy thin film powder X-ray diffraction pattern.

To understand the underlying properties of the different emissive states present in NaPy based on the molecular concentration, in the following, we study the temperature-dependent emission properties of the NaPy/PMMA thin films.

Figure 3 depicts the change in the emission properties between 300 K and 50 K for 1.7 mM NaPy/PMMA thin film. After an initial minor drop in quantum yield up to 240 K, the quantum yield increases by 17% over the initial value when the lowest temperature of 50 K is reached. No changes or shifts in the spectral features are observed other than a slight narrowing of the vibronic features. The fluorescence lifetimes are fit to a triexponential function, and the calculated amplitude-averaged weighted lifetimes concurrently slightly increase from 5.7 to 5.9 ns (Table 2, Table S3). This minor increase in quantum yield and lifetime is easily explained by the high inherent quantum yield of NaPy. We measure a quantum yield of 80% in solution. The relative quantum yield of the 1.7 mM NaPy/PMMA thin film is calculated at only 25%, however, slight H-type aggregation, solid-state outcoupling losses and scattering losses in the PMMA matrix are not considered in this calculation. Hence, to first approximation, we expect the isolated NaPy molecules in the PMMA matrix to behave similar to NaPy in solution and possess a high quantum yield. Therefore, the 17% increase in relative emission intensity would result in a near-unity quantum yield.

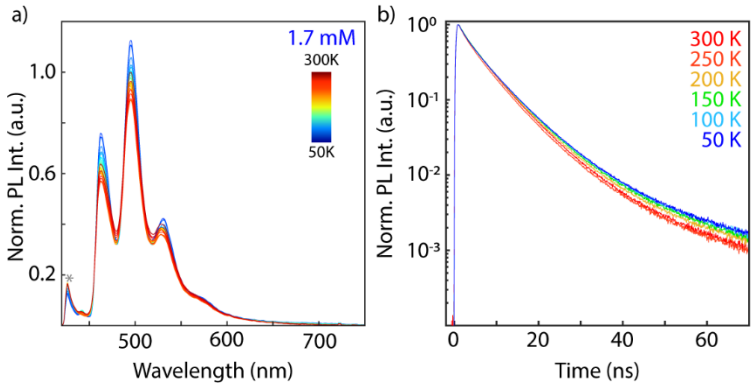

Figure 3: a) Temperature-dependent PL spectra for the 1.7 mM NaPy/PMMA thin film collected under 405 nm excitation (3 W cm^{-2}). The spectra are normalized to the 300 K spectrum, and spectra were in 10 K increments. b) PL decays for the 1.7 mM NaPy/PMMA film collected at selected temperatures collected under 405 nm pulsed excitation (1 MHz, 67 mW cm^{-2}).
Table 2 : Amplitude-weighted average lifetimes for the 1.7 mM NaPy/PMMA thin film based on a triexponential fit.

Temp /K	τ_{ave} / ns
300	5.7
250	5.4
200	5.8
150	5.9
100	5.8
50	5.9

Next, the temperature-dependent optical properties of the 8.3 mM NaPy/PMMA thin film are investigated (Figure 4). The temperature-dependent emission spectra are highlight in Figure 3a. Here, the emission spectrum can be reconstructed by linear combination of two basis spectra corresponding to a monomer-like emission spectrum which is slightly redshifted due to increased intermolecular coupling and a broad excimeric emission line shape (Figure 4b). Strong changes in the spectral shape with decreasing temperature are only expected if the excimer is formed through a thermally activated process over an activation barrier, as lowering the temperature reduces the available ambient thermal energy. However, as shown in Figure 4a, the spectral shape does not greatly change with temperature, only a sharpening of the vibronic feature is observed. Hence, we conclude there is no significant thermal activation barrier for excimer formation.

However, the overall photobrightening is much higher than previously observed for the monomer-like sample: 46%. The lower quantum yield of the excimer states allows for a much stronger suppression of detrimental non-radiative pathways and hence, photobrightening occurs to a greater extent (compare Figure S1). To separate the dynamics two emissive states, we show the recombination dynamics for wavelengths <500 nm (monomer dominate) and > 550 nm (excimer dominated) in Figure 4 c,d. In contrast to the emission lifetime for the monomer-like emission shown in Figure 3,

here, there is an addition early time component for the dynamics < 500 nm which can be attributed to intermolecular energy transfer. As observed previously for the 1.7 mM NaPy/PMMA sample, no distinct changes are observed for the monomer emission lifetime with temperature (the slightly longer lifetime of 250-300 K can be attributed to a higher fraction of overlapping excimer emission). However, the excimeric emission lifetime increases monotonically from 12.9 ns to 24.9 ns (Table 3, Table S4).

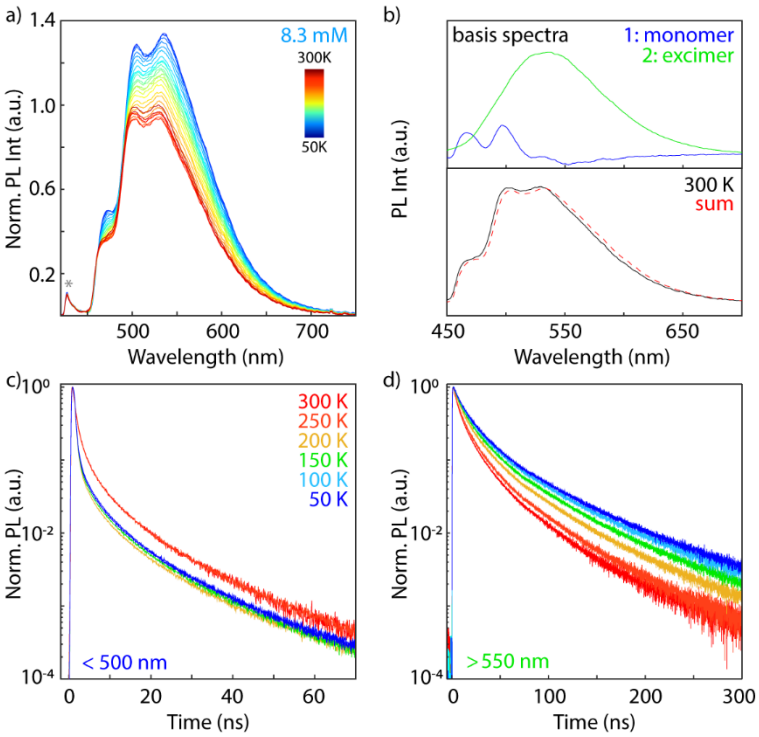

Figure 4: a) Temperature-dependent PL spectra for the 8.3 mM NaPy/PMMA thin film collected under 405 nm excitation (3 W cm^{-2}), normalized to the 300 K spectrum collected in 10 K increments. b) Spectral deconvolution (top) for the 300 K 8.3 mM NaPy/PMMA film into the underlying monomer-like (blue) and excimer-like (green) basis spectra. (bottom) Comparison for the collected 300 K spectra (black) and the sum of the first two basis spectra (red dashed). PL decays for the 8.3 mM NaPy/PMMA split into the monomer-like region (< 500 nm, c) and excimer-like region (> 550 nm, d) collected at selected temperatures. All decays were collected under 405 nm pulsed excitation (1MHz, 67 mW cm^{-2}).

Table 3: Amplitude-weighted average lifetimes for the excimer-like feature (> 550 nm) for the 8.3 mM NaPy/PMMA thin film based on a triexponential fit.

Temp /K	τ_{ave} / ns
300	12.9
250	14.3
200	18.3
150	21.0
100	23.5
50	24.9

Similar behavior is observed in the 16.5 mM NaPy/PMMA sample, which shows only excimer-type emission at all temperatures between 300K and 50K. As the temperature decreases, a simultaneous increase in the amplitude-weighted average emission lifetime from 10.6 to 18.3 ns (Figure 5 a,b, Table 4, Table S5) is observed. No noticeable shift in the emission wavelength with decreasing temperature is observed in agreement with the expected behavior of a localized excimeric state across two molecules. The highly multiexponential (or stretched exponential) nature of the decay is unsurprising due to the vast parameter space of local molecular arrangements possible in these inhomogeneous thin films.

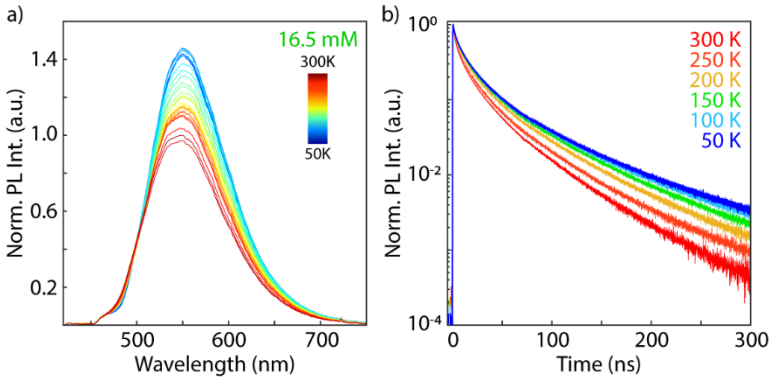

Figure 5: a) Temperature-dependent PL spectra for the 16.5 mM NaPy/PMMA thin film collected under 405 nm excitation (3 W cm^{-2}), normalized to the 300 K spectra collected in 10 K increments. b) PL decays for 16.5 mM NaPy/PMMA film collected at selected temperatures under 405 nm pulsed excitation (1 MHz, 67 mW cm^{-2}).

Table 4: Amplitude-weighted average lifetimes for the 16.5 mM NaPy/PMMA thin film based on a quadruple exponential fit and the fitting parameters for a stretched exponential fit $I(t) = A\exp(-(t/\tau)^c)$.

Temp /K	quadruple exponential	stretched exponential	
	τ_{ave} / ns	τ / ns	c
300	10.6	4.0	0.47
250	12.3	4.8	0.47
200	14.9	6.4	0.49
150	16.7	7.2	0.50
100	17.7	7.4	0.50
50	18.3	7.5	0.49

The temperature dependence of the fluorescence of the 18.2 mM NaPy/PMMA film is shown in Figure 6a. In contrast to the 16.5 mM NaPy/PMMA sample (Figure 5) which showed emission only from the excimer state, different spectral features are observed despite the minor increase in concentration: a slight amount of monomer emission below 520 nm and emission from the aggregate structure at ~520 nm. A continuous bathochromic shift of the aggregate emission is observed with decreasing temperature, as well as a strong enhancement of the fluorescence intensity. Below 100 K, a clear change in emission wavelength is observed with a corresponding linewidth broadening, indicating

that the underlying emissive state may be changing. An observation reminiscent of the dull state reported by Schmidt and co-workers for tetracene.[49] Interestingly, J-aggregates generally redshift with increasing temperatures due to increased exciton delocalization, not blueshift as observed here.[34,41] In agreement with the increased quantum yield upon cooling (~4-fold relative intensity increase), the amplitude-weighted average fluorescence lifetime increases from 1.3 ns at 300 K to 4.9 ns at 50K (Figure 6b, Table 5, Table S6). Noteworthy is that the overall shape of the decay dynamics is different at 50 K, which is agreement with the previously observed possible change in emissive state.

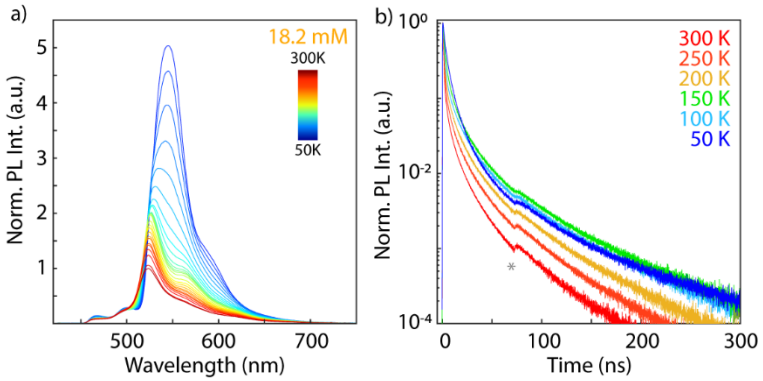

Figure 6: a) Temperature-dependent PL spectra for the 18.2 mM NaPy/PMMA thin film collected under 405 nm excitation (3 W cm^{-2}), normalized to the 300 K spectra collected in 10 K increments. b) PL decays for the 18.2 mM NaPy/PMMA film collected at selected temperatures under 405 nm pulsed excitation (1 MHz, 67 mW cm^{-2}). Asterisk denotes instrumental artifact.

Table 5: Amplitude-weighted average lifetimes for the 18.2 mM NaPy/PMMA thin film based on a triexponential fit.

Temp /K	τ_{ave} / ns
300	1.3
250	1.7
200	2.3
150	3.0
100	4.0
50	4.9

Further increasing the NaPy concentration to 24.8 mM results in the expected aggregate emission at 520 nm and the emergence of an additional emissive feature at 620 nm (Figure 7a) – the feature we have previously observed to be highly TTA-UC active contrary to the higher energy state.[28] Due to the fact that this feature has not been present in any of the other thin films which are all made from the same stock solution (vide infra), we can rule out contamination of NaPy to be the underlying cause of this redshifted emission.

With decreasing temperature, the high-energy aggregate state (520 nm) increases strongly in quantum yield and shifts to lower energies. In contrast to the 18.2 mM NaPy/PMMA thin film, the

redshift does not occur continuously with an apparent sudden concurrent broadening. Rather, the emission shoulder at 560 nm clearly increases in intensity with reducing temperature, while shifting toward higher energies (compare Figure S3).

The redshifted feature at 620 nm appears to disappear with decreasing temperature, possibly indicating a thermally activated population pathway, or it is simply dwarfed by the overwhelming intensity of the overlapping emission. The fluorescence decay dynamics for the two states are different, indicating that the emission stems from two distinct recombination pathways (Figure 7b,c) and not from the same state. The fluorescence lifetime of the high energy feature (isolated using a 550/40 center/width nm bandpass (BP) filter) strongly changes from an amplitude-weighted average lifetime of 1.1 ns at 300 K to 4.8 ns at 50 K. In contrast, the lifetime of the redshifted feature (taken with a 635/10 nm BP filter) only changes from 5.7 ns at 300 K to 10.1 ns at 50 K (Table 6, Table S7). This minor change should be taken with a grain of salt, some contribution of the underlying, blue-shifted emissive feature is not unexpected.

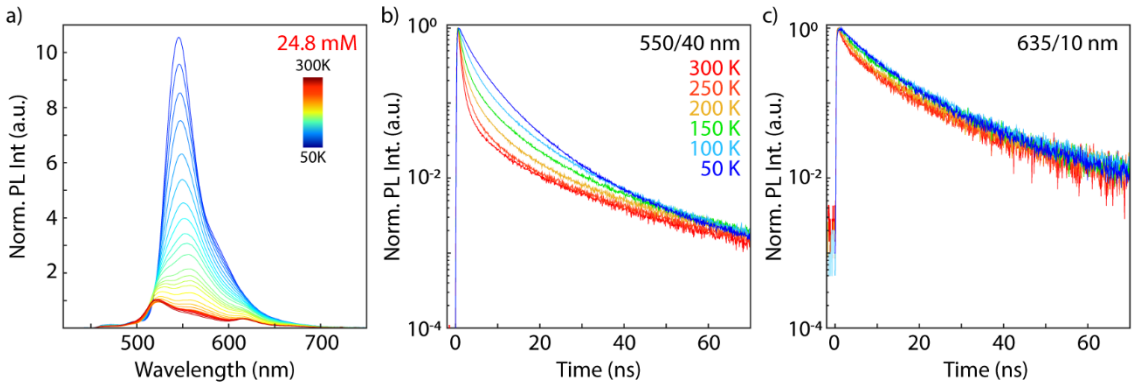

Figure 7: Temperature-dependent PL spectra for the 24.8 mM NaPy/PMMA thin film collected under 405 nm excitation (3 W cm^{-2}), normalized to the 300 K spectrum collected in 10 K increments. PL decays for the 24.8 mM NaPy/PMMA film collected under 405 nm pulsed excitation (1 MHz, 67 mW cm^{-2}) with a 550/40 nm BP filter (b) and 635/10 nm BP filter (c) at selected temperatures.

Table 6: Amplitude-weighted average lifetimes for the 24.8 mM NaPy/PMMA thin film based on triexponential fits.

Temp / K	τ_{ave} / ns 550 nm BP	τ_{ave} / ns 635 nm BP
300	1.1	5.7
250	1.3	6.7
200	1.8	8.3
150	2.3	9.3
100	2.8	10.5
50	4.8	10.1

Lastly, we show the temperature dependence of the 33.0 mM NaPy sample (Figure 8), which is spin-coated from the stock solution. Very similar to the previous 24.8 mM NaPy/PMMA film, the peak

emission redshifts and increases in intensity with decreasing temperature (Figure 8a), with a corresponding strong enhancement of the 560 nm emission. A close look at the rise time of the time-resolved emission supports a change in the emissive state: the peak emission is delayed by ~0.5 ns, indicating addition processes occurring prior to emission (Figure S5).

No shift in the emission wavelength for the feature at 620 nm is found, indicating no temperature dependence of the exciton localization – attributed to a localized state. The normalized temperature-dependent absorption is shown in Figure 8b, where only a sharpening of the absorption features is found. No absorption feature relating to the emission at 620 nm can be observed, indicating that this feature is present only in the excited state. The fluorescence lifetime increases for the high energy emission (0.5 ns at 300 K to 3.0 ns at 50 K), while the lifetime of the lower energy feature stays nearly constant with an initial monoexponential decay of ~8.3 ns (Figure 8c,d, Table 7, Table S8). To ensure that the shift in the emission is not caused by a change in the crystal structure of the NaPy, i.e., a phase transition, the temperature-dependent powder X-ray diffraction of NaPy is shown in Figure 8e. No additional reflections are observed as the temperature changes, only a shift of the reflections to higher angles 2θ as the temperature is decreased, corresponding to a lattice contraction. Based on the change in d-spacing with temperature, we extract a thermal expansion coefficient of approximately 4.24×10^{-4} Å/K and a relative expansion coefficient of approximately 30.69×10^{-6} K^{-1} between 110 and 300K (compare Figure S6 and Table S9).

Table 7: Extracted lifetimes for the 33.0 mM NaPy/PMMA temperature dependent PL decays based a triexponential fit (550/40 nm BP) and a monoexponential fit (635/10 nm BP).

Temp/K	550/40 nm BP	635/10 nm BP
	τ_{ave} / ns	τ / ns
300 K	0.5	8.2
250 K	1.0	8.1
200 K	1.1	8.3
150 K	2.1	8.5
100 K	3.6	8.4
50 K	3.0	8.2

This gives rise to two unanswered questions in the emission pathways of NaPy: i) what is causing the additional redshifted feature at 620 nm and ii) what is the type of aggregate present in NaPy? While previous reports have attributed the aggregate type of NaPy to a J-aggregate based on the redshifted absorption spectrum with respect to the monomeric spectrum, our results are at odds with the properties of a true J-aggregate. The redistribution of the oscillator strength resulting in a redshift of the absorption spectrum rules out the formation of an H-type aggregate; however, the redshift of the

emission upon cooling is unusual for a J-aggregate.[34] Hence, we conclude that this is better represented by an I-aggregate as described by Caram and co-workers:[34] both J- and H-type coupling are present, however, the J-type coupling is more dominant. The final indication that NaPy forms multidimensional I-aggregates is given in Figure 8b. The temperature-dependent absorption spectra show no shift in position with decreasing temperature, only a narrowing of the spectral features is found. In contrast, due to the curvature of the density of states, the J-aggregate absorption must redshift with decreasing temperature.[34]

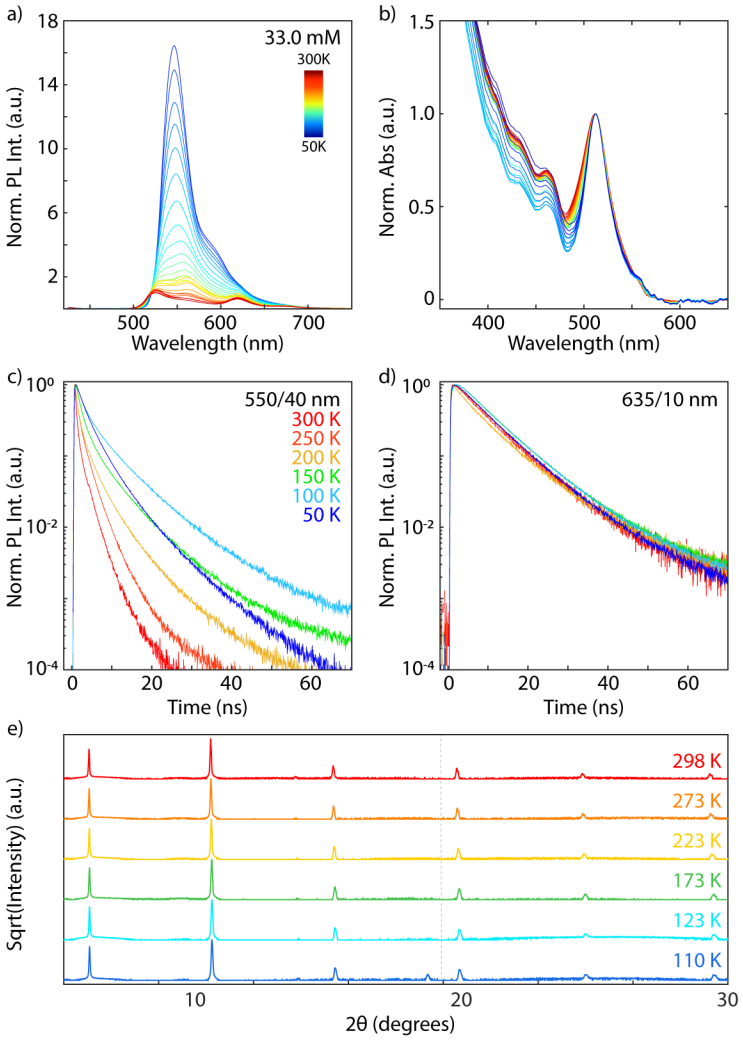

Figure 8: a) Temperature-dependent PL spectra for the 33.0 mM NaPy/PMMA thin film collected under 405 nm excitation (3 W cm^{-2}), normalized to the 300 K spectrum collected in 10 K increments. b) Normalized temperature-dependent absorbance spectra for the 33.0 mM NaPy/PMMA thin film collected every 10 K. Corresponding PL decays collected under 405 nm pulsed excitation (1 MHz, 67 mW cm^{-2}) with a 550/40 nm BP filter (c) and 635/10 nm BP filter (d) at selected temperatures. e) Normalized NaPy temperature dependent thin film diffraction patterns collected at selected temperatures. The dashed grey line is included as a guide to the eye.

This leads us to the discussion of the final mystery of NaPy - what is the additional redshifted emissive feature? We rule out the role of a coupled triplet pair state ^{1}(TT),[50,51] as the emission is present in air and it is significantly lowered with respect to the singlet state (~0.4 eV), making endothermic TTA-UC to the singlet state unlikely.[28] However, we do observe upconversion to this state, and subsequent emission, albeit weakly. Furthermore, such a low ^{1}(TT) state energy with respect to S_1 is at odds with previous reports of singlet fission in NaPy.[31]

Clearly, it is a strongly coupled state, resulting in a strong bathochromic shift of the emission. However, the corresponding absorption spectrum does not indicate an additional optical transition present for the ground state. Hence, we can conclude that similar to the excimer observed for the 16.5 mM NaPy/PMMA thin film, this is a purely excited state phenomenon. Excimeric-type emission is also in agreement with the relatively long-lived fluorescence lifetime. However, excimer emission is generally broad and featureless, hence, not in complete agreement with the observed emission spectrum. However, considering an ordered, strongly coupled J-dimer, where the emission is delocalized over exactly two molecules, vibronic structure has been observed.[42,43] Another indication that this emission does not stem from a delocalized state is found in the temperature-dependent properties of its emission. In contrast to the main aggregate emission at 520 nm, this redshifted feature at 620 nm does not shift with decreasing temperature, indicating that the wavefunction delocalization is not dependent on temperature. Hence, we conclude that this additional feature is caused by a strongly coupled localized J-dimer or a J-type excimer, which can be thought of as a local structural defect which results in strong interactions between the molecules.

SUMMARY AND OUTLOOK

In summary, our results indicate that NaPy has several different emissive states dependent on the local environment of the NaPy molecules. At low concentrations, we observe monomer-like emission. With increasing NaPy concentration, i.e., increasing intermolecular interactions, excimeric emission appears. Upon further increase in concentration, ordered I-aggregates are formed, and an additional increase in concentration results in emission from J-dimers.

The temperature-dependent optical properties are summarized in Figure 8a. In addition, Figure 8b shows the spectral composition of the solid-state NaPy spectrum based on the individual emissive states present: I-aggregate, excimer and J-dimer.

Lastly, we discuss these results in context of our previous results on perovskite-sensitized upconversion in NaPy.[25,28] Our results indicated that there was a change in the dominant emissive

feature, depending upon whether NaPy was directly excited or emission was the result of charge injection from a lead halide perovskite to the triplet state of the NaPy molecule.[28] Two underlying reasons are possible. We had previously hypothesized that the lowered energy of this emissive state results in energetically favored upconversion, with no detrimental effects of possible singlet fission, while the higher energy I-aggregate state may only be accessible through thermal excitation or through entropic effects. However, considering the strongly coupled nature of the J-dimer and the unfavorable singlet fission from this feature, the J-dimers may act as hotspots for preferential triplet-triplet annihilation – strong coupling should result in a favorable annihilation process. Lastly, the J-dimer may also be able to act as a triplet trap, facilitating the upconversion process.

In conclusion, we have investigated the optical properties of NaPy as a function of temperature and local environment. We find that intermolecular interactions tune the emission of NaPy from its molecular emission spectrum through an excimer emission to an I-aggregate emission. J-dimer emission is observed in the bulk, and we hypothesize that the strongly coupled nature of this localized state facilitates photon upconversion in this molecule.

MATERIALS AND METHODS

Device Synthesis

Glass substrates were cleaned *via* sonication for 15 min in each of the respective solutions: 2 % Hellmanex, deionized water, and acetone. Following sonication, the substrates were cleaned via UV-ozone (Ossila) treatment.

Naphtho(2,3-a)pyrene (NaPy >98%, TCI) and polymethylmethacrylate (PMMA, Sigma Aldrich) were used without further purification. Stock solutions of 10 mg/mL of NaPy in anhydrous toluene (Sigma-Aldrich) and a 3% *w/w* PMMA solution in anhydrous toluene (Sigma-Aldrich) were prepared. The different concentrations of NaPy/PMMA thin films were prepared through appropriate dilutions, then spin coated at 6000 rpm. Films were encapsulated with a cover slip using a two-part epoxy (Devcon) under an inert nitrogen atmosphere (<0.5 ppm O_2) prior to removal from the glovebox.

Films for the temperature dependent X-ray diffraction measurements were prepared as described and drop cast onto sapphire in order to minimize background scattering.

Temperature Control

Temperature control for all steady-state and time-resolved emission experiments were collected using a He-filled cryocooler (Air Products). The encapsulated films were mounted onto a cold-finger optical sample mount prior to sheath evacuation (~10^{-5} mBar). A PID Digital Temperature Controller

Model 9650 (Scientific Instruments) was used to maintain the desired temperature. The cold-finger was left to equilibrate for approximately 1 min prior to collecting absorbance and PL spectra for each temperature point.

Steady-State Absorption Spectroscopy

A Thermo Scientific Evolution 220 Spectrophotometer was used for all absorption spectra.

Steady-State Emission Spectroscopy

Direct excitation emission spectra were collected with a 405 nm continuous wave laser (LDH-D-C-405, PicoQuant) at a power density of 30 W/cm^2 for the room temperature NaPy/PMMA measurements and 3 W cm^{-2} for the temperature dependent measurements. A 425 nm long-pass filter (Chroma Tech) to remove excess laser scattering. An Ocean Insight emission spectrometer (HR2000+ES) was used to collect all spectra.

Time-Resolved Emission Spectroscopy

NaPy photoluminescence (PL) decays were measured through time-correlated single photon counting (TCSPC) with a 405 nm picosecond pulsed laser (LDH-D-C-405, PicoQuant) with a 1 MHz repetition frequency at a power density of 64.9 mW cm^{-2} for the room temperature spectra and 67 mW cm^{-2} for the temperature dependent measurements. A 425 nm long-pass filter (Chroma Tech) was used to remove laser scatter. To isolate the underlying spectral features, a 500 nm short pass (ThorLabs), 550 nm long pass (ThorLabs), 550 nm bandpass (FWHM = 40 nm, ThorLabs), and 635 nm bandpass (FWHM = 10 nm, ThorLabs) filters were used. A HydraHarp 400 event timer (PicoQuant) connected to a single-photon avalanche photodiode (Micro Photon Devices) was used to collect photon arrival times for all measurements. Laser powers were measured with a silicon power meter (PM100-D, ThorLabs), and spot sizes were calculated using the razor blade method (90:10).

Single Crystal Diffraction

Single crystal diffraction was carried out using a STOE Stadivari 4-circle diffractometer equipped with a Dectris Eiger detector and an Oxford Cryostream 1000. The measurement temperature was 150 K. The data collection used the X-Area program suite [reference X-Area Single Crystals Diffraction Software, Version 2.1, STOE & Cie GmbH, Darmstadt (2022)], and the refinements used the program suite CRYSTALS.[52]

Powder X-ray Diffraction

X-ray powder patterns were acquired using an Anton Paar XRDynamic 500 powder diffractometer equipped with the CHC Plus+ Cryo & Humidity Chamber and a Bragg-Brentano monochromator. The diffractometer was configured with liquid nitrogen cooling and operated under vacuum conditions.

The cooling rate was maintained at 20 K per minute. Powder pattern measurements were taken at ambient temperature (298 K), 273 K, 223 K, 173 K, 1123 K and 110 K and once again at ambient temperature following the lowest temperature scan. The measurements were performed with Cu Kα radiation, using a step size of 0.01 ° from 5 to 40 ° 2θ at 200.691 seconds per step.

Scanning Electron Microscopy

Samples were platinum-coated (3 nm) prior to analysis. High-resolution imaging was conducted using a Tescan MIRA 4 field emission scanning electron microscope (FE SEM). Imaging was performed with secondary electrons (SE) and in-beam SE detectors at an accelerating voltage of 5 kV.

ASSOCIATED CONTENT

Supporting Information.

Supporting figures containing additional optical spectroscopy, XRD pattern comparisons, SEM-SE micrographs and thermal expansion coefficient fits. Supporting tables listing the fit parameters for the PL decays, single crystal unit cell parameters and the d-spacings at the different temperatures.

Data Availability

Raw data files are available at DOI: 10.17605/OSF.IO/S276H

AUTHOR INFORMATION

Corresponding Author

*E-mail: nienhaus@rice.edu

Notes

The authors declare no conflict of interest.

ACKNOWLEDGEMENTS

C.M.S. and L.N. acknowledge funding by the National Science Foundation under Grant No. DMR-2237977 and support by the Camille and Henry Dreyfus Foundation (TC-23-050). T.S. acknowledges funding by the National Science Foundation under Grant No. DMR-2219906. T.S. and A.M.S. performed part of the work at the National High Magnetic Field Laboratory, which is supported by the National Science Foundation under Grant DMR-2128556 and the State of Florida.

REFERENCES

(1) Hu, M.; Belliveau, E.; Wu, Y.; Narayanan, P.; Feng, D.; Hamid, R.; Murrietta, N.; Ahmed, G. H.; Kats, M. A.; Congreve, D. N. Bulk Heterojunction Upconversion Thin Films Fabricated via One-Step Solution Deposition. *ACS Nano* **2023**, *17* (22), 22642–22655. https://doi.org/10.1021/acsnano.3c06955.

(2) Alves, J.; Feng, J.; Nienhaus, L.; Schmidt, T. W. Challenges, Progress and Prospects in Solid State Triplet Fusion Upconversion. *J. Mater. Chem. C* **2022**, *10* (20), 7783–7798. https://doi.org/10.1039/D1TC05659J.

(3) Amemori, S.; Sasaki, Y.; Yanai, N.; Kimizuka, N. Near-Infrared-to-Visible Photon Upconversion Sensitized by a Metal Complex with Spin-Forbidden yet Strong S_0–T_1 Absorption. *J. Am. Chem. Soc.* **2016**, *138* (28), 8702–8705. https://doi.org/10.1021/jacs.6b04692.

(4) Mase, K.; Okumura, K.; Yanai, N.; Kimizuka, N. Triplet Sensitization by Perovskite Nanocrystals for Photon Upconversion. *Chem. Commun.* **2017**, *53* (59), 8261–8264. https://doi.org/10.1039/C7CC03087H.

(5) Huang, Z.; Xu, Z.; Mahboub, M.; Li, X.; Taylor, J. W.; Harman, W. H.; Lian, T.; Tang, M. L. PbS/CdS Core–Shell Quantum Dots Suppress Charge Transfer and Enhance Triplet Transfer. *Angew. Chem.* **2017**, *129* (52), 16810–16814. https://doi.org/10.1002/ange.201710224.

(6) Luo, X.; Han, Y.; Chen, Z.; Li, Y.; Liang, G.; Liu, X.; Ding, T.; Nie, C.; Wang, M.; Castellano, F. N.; Wu, K. Mechanisms of Triplet Energy Transfer across the Inorganic Nanocrystal/Organic Molecule Interface. *Nat. Commun.* **2020**, *11* (1), 28. https://doi.org/10.1038/s41467-019-13951-3.

(7) Garakyaraghi, S.; Mongin, C.; Granger, D. B.; Anthony, J. E.; Castellano, F. N. Delayed Molecular Triplet Generation from Energized Lead Sulfide Quantum Dots. *J. Phys. Chem. Lett.* **2017**, *8* (7), 1458–1463. https://doi.org/10.1021/acs.jpclett.7b00546.

(8) Schmidt, T.; Gholizadeh, E.; Prasad, S.; Teh, Z. L.; Ishwara, T.; Norman, S.; Petty, A. J.; Anthony, J. E.; Huang, S. Oxygen-Enhanced Upconversion of Near Infrared Light from Below the Silicon Band Gap. **2019**, https://doi.org/10.26434/chemrxiv.7834838.v1.

(9) Cheng, Y. Y.; Khoury, T.; Clady, R. G. C. R.; Tayebjee, M. J. Y.; Ekins-Daukes, N. J.; Crossley, M. J.; Schmidt, T. W. On the Efficiency Limit of Triplet–Triplet Annihilation for Photochemical Upconversion. *Phys. Chem. Chem. Phys.* **2010**, *12* (1), 66–71. https://doi.org/10.1039/B913243K.

(10) Schmidt, T. W.; Castellano, F. N. Photochemical Upconversion: The Primacy of Kinetics. *J. Phys. Chem. Lett.* **2014**, *5* (22), 4062–4072. https://doi.org/10.1021/jz501799m.

(11) Han, Y.; Luo, X.; Lai, R.; Li, Y.; Liang, G.; Wu, K. Visible-Light-Driven Sensitization of Naphthalene Triplets Using Quantum-Confined CsPbBr3 Nanocrystals. *J. Phys. Chem. Lett.* **2019**, *10* (7), 1457–1463. https://doi.org/10.1021/acs.jpclett.9b00597.

(12) He, S.; Luo, X.; Liu, X.; Li, Y.; Wu, K. Visible-to-Ultraviolet Upconversion Efficiency above 10% Sensitized by Quantum-Confined Perovskite Nanocrystals. *J. Phys. Chem. Lett.* **2019**, *10* (17), 5036–5040. https://doi.org/10.1021/acs.jpclett.9b02106.

(13) Bender, J. A.; Raulerson, E. K.; Li, X.; Goldzak, T.; Xia, P.; Van Voorhis, T.; Tang, M. L.; Roberts, S. T. Surface States Mediate Triplet Energy Transfer in Nanocrystal–Acene Composite Systems. *J. Am. Chem. Soc.* **2018**, *140* (24), 7543–7553. https://doi.org/10.1021/jacs.8b01966.

(14) Huang, Z.; Tang, M. L. Designing Transmitter Ligands That Mediate Energy Transfer between Semiconductor Nanocrystals and Molecules. *J. Am. Chem. Soc.* **2017**, *139* (28), 9412–9418. https://doi.org/10.1021/jacs.6b08783.

(15) Sullivan, C. M.; Bieber, A. S.; Drozdick, H. K.; Moller, G.; Kuszynski, J. E.; VanOrman, Z. A.; Wieghold, S.; Strouse, G. F.; Nienhaus, L. Surface Doping Boosts Triplet Generation Yield in

Perovskite-Sensitized Upconversion. *Adv. Opt. Mater.* **2023**, *11* (1), 2201921. https://doi.org/10.1002/adom.202201921.
(16) Nienhaus, L.; Correa-Baena, J.-P.; Wieghold, S.; Einzinger, M.; Lin, T.-A.; Shulenberger, K. E.; Klein, N. D.; Wu, M.; Bulović, V.; Buonassisi, T.; Baldo, M. A.; Bawendi, M. G. Triplet-Sensitization by Lead Halide Perovskite Thin Films for Near-Infrared-to-Visible Upconversion. *ACS Energy Lett.* **2019**, 888–895. https://doi.org/10.1021/acsenergylett.9b00283.
(17) Wang, L.; Yoo, J. J.; Lin, T.-A.; Perkinson, C. F.; Lu, Y.; Baldo, M. A.; Bawendi, M. G. Interfacial Trap-Assisted Triplet Generation in Lead Halide Perovskite Sensitized Solid-State Upconversion. *Adv. Mater.* **2021**, *33* (27), 2100854. https://doi.org/10.1002/adma.202100854.
(18) Prashanthan, K.; Naydenov, B.; Lips, K.; Unger, E.; MacQueen, R. W. Interdependence of Photon Upconversion Performance and Antisolvent Processing in Thin-Film Halide Perovskite-Sensitized Triplet–Triplet Annihilators. *J. Chem. Phys.* **2020**, *153* (16), 164711. https://doi.org/10.1063/5.0026564.
(19) Nienhaus, L.; Wu, M.; Geva, N.; Shepherd, J. J.; Wilson, M. W. B.; Bulović, V.; Van Voorhis, T.; Baldo, M. A.; Bawendi, M. G. Speed Limit for Triplet-Exciton Transfer in Solid-State PbS Nanocrystal-Sensitized Photon Upconversion. *ACS Nano* **2017**, *11* (8), 7848–7857. https://doi.org/10.1021/acsnano.7b02024.
(20) Wu, M.; Congreve, D. N.; Wilson, M. W. B.; Jean, J.; Geva, N.; Welborn, M.; Van Voorhis, T.; Bulović, V.; Bawendi, M. G.; Baldo, M. A. Solid-State Infrared-to-Visible Upconversion Sensitized by Colloidal Nanocrystals. *Nat. Photonics* **2016**, *10* (1), 31–34. https://doi.org/10.1038/nphoton.2015.226.
(21) Wu, M.; Jean, J.; Bulović, V.; Baldo, M. A. Interference-Enhanced Infrared-to-Visible Upconversion in Solid-State Thin Films Sensitized by Colloidal Nanocrystals. *Appl. Phys. Lett.* **2017**, *110* (21), 211101. https://doi.org/10.1063/1.4984136.
(22) Wieghold, S.; Bieber, A. S.; VanOrman, Z. A.; Rodriguez, A.; Nienhaus, L. Is Disorder Beneficial in Perovskite-Sensitized Solid-State Upconversion? Role of DBP Doping in Rubrene. *J. Phys. Chem. C* **2020**, *124* (33), 18132–18140. https://doi.org/10.1021/acs.jpcc.0c05290.
(23) Duan, J.; Liu, Y.; Zhang, Y.; Chen, Z.; Xu, X.; Ye, L.; Wang, Z.; Yang, Y.; Zhang, D.; Zhu, H. Efficient Solid-State Infrared-to-Visible Photon Upconversion on Atomically Thin Monolayer Semiconductors. *Sci. Adv. 8* (43), eabq4935. https://doi.org/10.1126/sciadv.abq4935.
(24) Radiunas, E.; Dapkevičius, M.; Raišys, S.; Juršėnas, S.; Jozeliūnaitė, A.; Javorskis, T.; Šinkevičiūtė, U.; Orentas, E.; Kazlauskas, K. Impact of T-Butyl Substitution in a Rubrene Emitter for Solid State NIR-to-Visible Photon Upconversion. *Phys. Chem. Chem. Phys.* **2020**, *22* (14), 7392–7403. https://doi.org/10.1039/D0CP00144A.
(25) Wieghold, S.; Bieber, A. S.; VanOrman, Z. A.; Daley, L.; Leger, M.; Correa-Baena, J.-P.; Nienhaus, L. Triplet Sensitization by Lead Halide Perovskite Thin Films for Efficient Solid-State Photon Upconversion at Subsolar Fluxes. *Matter* **2019**, *1*, 705–719. https://doi.org/10.1016/j.matt.2019.05.026.
(26) Sullivan, C. M.; Nienhaus, L. Recharging Upconversion: Revealing Rubrene's Replacement. *Nanoscale* **2022**, *14* (46), 17254–17261. https://doi.org/10.1039/D2NR05309H.
(27) Sullivan, C. M.; Nienhaus, L. Generating Spin-Triplet States at the Bulk Perovskite/Organic Interface for Photon Upconversion. *Nanoscale* **2023**, *15* (3), 998–1013. https://doi.org/10.1039/D2NR05767K.
(28) Sullivan, C. M.; Nienhaus, L. Turning on TTA: Tuning the Energy Landscape by Intermolecular Coupling. *Chem. Mater.* **2024**, *36* (1), 417–424. https://doi.org/10.1021/acs.chemmater.3c02349.

(29) France, C. B.; Parkinson, B. A. Chiral Morphologies and Interfacial Electronic Structure of Naphtho[2,3-a]Pyrene on Au(111). *Langmuir* **2004**, *20* (7), 2713–2719. https://doi.org/10.1021/la035532i.
(30) France, C. B.; Parkinson, B. A. Naphtho[2,3-a]Pyrene Forms Chiral Domains on Au(111). *J. Am. Chem. Soc.* **2003**, *125* (42), 12712–12713. https://doi.org/10.1021/ja037056o.
(31) Aggarwal, N.; Patnaik, A. Dimeric Conformation Sensitive Electronic Excited States of Tetracene Congeners and Their Unconventional Non-Fluorescent Behaviour. *J. Chem. Sci.* **2019**, *131* (6), 52. https://doi.org/10.1007/s12039-019-1626-5.
(32) Bae, Y. J.; Kang, G.; Malliakas, C. D.; Nelson, J. N.; Zhou, J.; Young, R. M.; Wu, Y.-L.; Van Duyne, R. P.; Schatz, G. C.; Wasielewski, M. R. Singlet Fission in 9,10-Bis(Phenylethynyl)Anthracene Thin Films. *J. Am. Chem. Soc.* **2018**, *140* (45), 15140–15144. https://doi.org/10.1021/jacs.8b07498.
(33) Charbr, M.; Williams, D. F. Singlet Exciton Trapping and Heterofission in Tetracene Doped Anthracene Crystals. *Chem. Phys. Lett.* **1977**, *49* (3), 599–603. https://doi.org/10.1016/0009-2614(77)87048-6.
(34) Deshmukh, A. P.; Geue, N.; Bradbury, N. C.; Atallah, T. L.; Chuang, C.; Pengshung, M.; Cao, J.; Sletten, E. M.; Neuhauser, D.; Caram, J. R. Bridging the Gap between H- and J-Aggregates: Classification and Supramolecular Tunability for Excitonic Band Structures in Two-Dimensional Molecular Aggregates. *Chem. Phys. Rev.* **2022**, *3* (2), 021401. https://doi.org/10.1063/5.0094451.
(35) Lim, S.-H.; Bjorklund, T. G.; Spano, F. C.; Bardeen, C. J. Exciton Delocalization and Superradiance in Tetracene Thin Films and Nanoaggregates. *Phys. Rev. Lett.* **2004**, *92* (10), 107402. https://doi.org/10.1103/PhysRevLett.92.107402.
(36) Lin, K.-Y.; Wang, Y.-J.; Chen, K.-L.; Ho, C.-Y.; Yang, C.-C.; Shen, J.-L.; Chiu, K.-C. Role of Molecular Conformations in Rubrene Polycrystalline Films Growth from Vacuum Deposition at Various Substrate Temperatures. *Sci. Rep.* **2017**, *7* (1), 40824. https://doi.org/10.1038/srep40824.
(37) Greenwell, C.; Beran, G. J. O. Rubrene Untwisted: Common Density Functional Theory Calculations Overestimate Its Deviant Tendencies. *J. Mater. Chem. C* **2021**, *9* (8), 2848–2857. https://doi.org/10.1039/D0TC05463A.
(38) Mukherjee, T.; Sinha, S.; Mukherjee, M. Electronic Structure of Twisted and Planar Rubrene Molecules: A Density Functional Study. *Phys. Chem. Chem. Phys.* **2018**, *20* (27), 18623–18629. https://doi.org/10.1039/C8CP02318B.
(39) Volek, T. S.; Armstrong, Z. T.; Sowa, J. K.; Wilson, K. S.; Bohlmann Kunz, M.; Bera, K.; Koble, M.; Frontiera, R. R.; Rossky, P. J.; Zanni, M. T.; Roberts, S. T. Structural Disorder at the Edges of Rubrene Crystals Enhances Singlet Fission. *J. Phys. Chem. Lett.* **2023**, *14* (50), 11497–11505. https://doi.org/10.1021/acs.jpclett.3c02845.
(40) Spano, F. C.; Silva, C. H- and J-Aggregate Behavior in Polymeric Semiconductors. *Annu. Rev. Phys. Chem.* **2014**, *65* (1), 477–500. https://doi.org/10.1146/annurev-physchem-040513-103639.
(41) Hestand, N. J.; Spano, F. C. Expanded Theory of H- and J-Molecular Aggregates: The Effects of Vibronic Coupling and Intermolecular Charge Transfer. *Chem. Rev.* **2018**, *118* (15), 7069–7163. https://doi.org/10.1021/acs.chemrev.7b00581.
(42) Tian, D.; Qi, F.; Ma, H.; Wang, X.; Pan, Y.; Chen, R.; Shen, Z.; Liu, Z.; Huang, L.; Huang, W. Domino-like Multi-Emissions across Red and near Infrared from Solid-State 2-/2,6-Aryl Substituted BODIPY Dyes. *Nat. Commun.* **2018**, *9* (1), 2688. https://doi.org/10.1038/s41467-018-05040-8.
(43) Musser, A. J.; Rajendran, S. K.; Georgiou, K.; Gai, L.; Grant, R. T.; Shen, Z.; Cavazzini, M.; Ruseckas, A.; Turnbull, G. A.; Samuel, I. D. W.; Clark, J.; Lidzey, D. G. Intermolecular States in Organic Dye Dispersions: Excimers vs. Aggregates. *J. Mater. Chem. C* **2017**, *5* (33), 8380–8389. https://doi.org/10.1039/C7TC02655B.

(44) Hoche, J.; Schmitt, H.-C.; Humeniuk, A.; Fischer, I.; Mitrić, R.; Röhr, M. I. S. The Mechanism of Excimer Formation: An Experimental and Theoretical Study on the Pyrene Dimer. *Phys. Chem. Chem. Phys.* **2017**, *19* (36), 25002–25015. https://doi.org/10.1039/C7CP03990E.
(45) Dimitriev, O. P.; Piryatinski, Y. P.; Slominskii, Y. L. Excimer Emission in J-Aggregates. *J. Phys. Chem. Lett.* **2018**, *9* (9), 2138–2143. https://doi.org/10.1021/acs.jpclett.8b00481.
(46) Cho, D. W.; Cho, D. W. Excimer and Exciplex Emissions of 1,8-Naphthalimides Caused by Aggregation in Extremely Polar or Nonpolar Solvents. *New J. Chem.* **2014**, *38* (6), 2233–2236. https://doi.org/10.1039/C3NJ01473H.
(47) Abd-El-Aziz, A. S.; Abdelghani, A. A.; Wagner, B. D.; Abdelrehim, E. M. Aggregation Enhanced Excimer Emission (AEEE) with Efficient Blue Emission Based on Pyrene Dendrimers. *Polym. Chem.* **2016**, *7* (19), 3277–3299. https://doi.org/10.1039/C6PY00443A.
(48) Deshmukh, A. P.; Koppel, D.; Chuang, C.; Cadena, D. M.; Cao, J.; Caram, J. R. Design Principles for Two-Dimensional Molecular Aggregates Using Kasha's Model: Tunable Photophysics in Near and Short-Wave Infrared. *J. Phys. Chem. C* **2019**, *123* (30), 18702–18710. https://doi.org/10.1021/acs.jpcc.9b05060.
(49) Tayebjee, M. J. Y.; Clady, R. G. C. R.; Schmidt, T. W. The Exciton Dynamics in Tetracene Thin Films. *Phys. Chem. Chem. Phys.* **2013**, *15* (35), 14797–14805. https://doi.org/10.1039/C3CP52609G.
(50) Yong, C. K.; Musser, A. J.; Bayliss, S. L.; Lukman, S.; Tamura, H.; Bubnova, O.; Hallani, R. K.; Meneau, A.; Resel, R.; Maruyama, M.; Hotta, S.; Herz, L. M.; Beljonne, D.; Anthony, J. E.; Clark, J.; Sirringhaus, H. The Entangled Triplet Pair State in Acene and Heteroacene Materials. *Nat. Commun.* **2017**, *8* (1), 15953. https://doi.org/10.1038/ncomms15953.
(51) Stern, H. L.; Cheminal, A.; Yost, S. R.; Broch, K.; Bayliss, S. L.; Chen, K.; Tabachnyk, M.; Thorley, K.; Greenham, N.; Hodgkiss, J. M.; Anthony, J.; Head-Gordon, M.; Musser, A. J.; Rao, A.; Friend, R. H. Vibronically Coherent Ultrafast Triplet-Pair Formation and Subsequent Thermally Activated Dissociation Control Efficient Endothermic Singlet Fission. *Nat. Chem.* **2017**, *9* (12), 1205–1212. https://doi.org/10.1038/nchem.2856.
(52) Betteridge, P. W.; Carruthers, J. R.; Cooper, R. I.; Prout, K.; Watkin, D. J. It CRYSTALS Version 12: Software for Guided Crystal Structure Analysis. *J. Appl. Crystallogr.* **2003**, *36* (6), 1487. https://doi.org/10.1107/S0021889803021800.